

# Interfacial Reactions in Model NiTi Shape Memory Alloy Fiber-Reinforced Sn Matrix “Smart” Composites

J.P. COUGHLIN, J.J. WILLIAMS, G.A. CRAWFORD, and N. CHAWLA

In this article, the microstructure properties of a novel Pb-free solder composite were examined. A binary nickel-titanium shape memory alloy (SMA) fiber was used to reinforce the Sn-rich matrix, to take advantage of the superelastic properties of the fiber. The objective of this study was to understand long-term, high-temperature interfacial growth in a model NiTi fiber-reinforced Sn matrix composite solder system. The microstructure was quantified by scanning electron microscopy (SEM), energy dispersive spectroscopy (EDS), and wavelength dispersive spectroscopy (WDS). The mechanical properties of the interfacial zone, *e.g.*, Young's modulus and hardness, were characterized by nanoindentation. The evolution of the reaction products with time and the relationship between composition and local mechanical properties are discussed.

DOI: 10.1007/s11661-008-9676-1

© The Minerals, Metals & Materials Society and ASM International 2008

## I. INTRODUCTION

HEALTH concerns over Pb toxicity in traditional Pb-Sn solders have prompted the need for Pb-free solders in electronic packaging.<sup>[1-3]</sup> In general, Sn-rich solder alloys based on binary and ternary eutectics of Ag and Cu exhibit significant advantages in creep and thermal fatigue resistance over Pb-Sn solders.<sup>[4-6]</sup> However, these replacement alloys exhibit inferior ductility to Pb-Sn alloys. When these solder joints are subjected to mechanical stress during assembly, packaging, or in service, the poor ductility may result in failure of the component.<sup>[7,8]</sup>

The damage tolerance of these solder alloys may be improved by adding shape memory alloy (SMA) fibers to the Sn-rich solder matrix. Shape memory alloys exhibit excellent damage tolerance, up to strains as high as 10 pct with no significant degree of permanent deformation. This is accomplished *via* two-phase-transformation mechanisms: (a) superelastic transformation and (b) thermally induced transformation.<sup>[10]</sup> The superelastic transformation occurs when the SMA is strained above the austenite start temperature and transforms from austenite to martensite. After the sample is loaded above the critical transformation stress of the alloy, strain can be recovered simply by unloading and it reverts back to austenite.<sup>[9,10]</sup> For the thermally induced transformation, plastic deformation can be

recovered upon the application of heat, as the material returns to its original dimensions. A superelastic transformation may be desirable in a Pb-free solder composite, because it does not require a heating cycle to recover deformation. Thus, if the SMA/solder composites are subjected to an external stress along the direction of the wire, a superelastic transformation will occur in the SMA fibers. When the external stress is removed, the SMA fibers should return to their original dimensions.

The NiTi SMAs are a good choice as reinforcement in composites due to their relatively low cost and unique properties.<sup>[11-19]</sup> Binary 50-50 at. pct NiTi alloys can have transformation temperatures just below 0 °C and a superelastic range between freezing and 250 °C, making them excellent candidates for consumer electronics. When considering NiTi fiber-reinforced Sn matrix composites, the microstructure and properties of the interface between the solder and SMA fibers are very important. Bond strength between the matrix and reinforcement must be strong enough to provide load transfer, which is directly dependent on interfacial growth characteristics of the materials in the system. Therefore, it is necessary to have an in-depth understanding of interfacial reactions that take place during melting of the solder (liquid Sn) and NiTi.

The microstructure of NiTi fiber/solder composites has not been studied in detail.<sup>[19-23]</sup> Dutta and co-workers<sup>[20]</sup> fabricated Sn-3.8Ag-0.7Cu solder with a single 1-mm-diameter NiTi fiber and a fiber volume fraction of about 11 pct, cast at 533 K. It was originally reported that an intermetallic of Ni<sub>3</sub>Sn<sub>4</sub> was observed at the NiTi wire/solder interface for a Sn-rich sample held at the reflow temperature of 533 K for approximately 3 minutes. This analysis was reversed in subsequent articles,<sup>[21,22]</sup> where they identified a small reaction zone, *via* energy dispersive spectroscopy (EDS) line-scan analysis, consisting of interdiffused Sn and Ti. A clear understanding of the interaction between NiTi and Sn is

---

J.P. COUGHLIN, formerly Graduate Research Assistant, School of Materials, Fulton School of Engineering, Arizona State University, is Engineer with the Assembly Technology Division, Intel Corporation, Chandler, AZ 85224. J.J. WILLIAMS, Research Scientist, and G.A. CRAWFORD, Ph.D. Student, are with the School of Materials, Fulton School of Engineering, Arizona State University. N. CHAWLA, Professor, School of Materials and Department of Mechanical and Aerospace Engineering, is with Arizona State University, Tempe, AZ 85287-8706. Contact e-mail: nchawla@asu.edu

Manuscript submitted March 27, 2008.

Article published online October 25, 2008

required. The objective of this study is to understand long-term, high-temperature interfacial growth in a model NiTi fiber-reinforced Sn matrix composite solder system. The microstructure was quantified by scanning electron microscopy (SEM), EDS, and wavelength dispersive spectroscopy (WDS). The mechanical properties of the interfacial zone, *e.g.*, Young's modulus and hardness, were characterized by nanoindentation.

## II. MATERIALS AND EXPERIMENTAL PROCEDURE

Commercial NiTi wire (Memry Corporation, Bethel, CT), approximately 600  $\mu\text{m}$  in diameter, was used in this study. The wire was cold drawn, guide wire straightened, and annealed at 850  $^{\circ}\text{C}$  for 30 minutes followed by a water quench by the manufacturer. Differential scanning calorimetry was performed on the NiTi fiber to determine transformation temperatures. A schematic of the fabrication process for making the model single fiber composites is shown in Figure 1. The fiber was etched in an aqueous solution containing 4.8 pct HF and 10.5 pct  $\text{HNO}_3$  for 5 minutes to remove surface oxides. Pure Sn was melted in a tapered porcelain crucible at 300  $^{\circ}\text{C}$ . The wire was dipped in a phosphoric acid-based flux (Indalloy flux 2, Indium Corporation, Utica, NY) and placed upright on a hot

plate for 1 minute to raise the temperature of the flux to approximately 100  $^{\circ}\text{C}$ . The wire was then immersed in liquid Sn and aged for up to 168 hours at 300  $^{\circ}\text{C}$  in a furnace. After aging, the samples were removed from the furnace and air cooled on an  $\text{Al}_2\text{O}_3$  block.

In order to characterize the microstructure, samples were sectioned perpendicular to the fiber direction and polished to a final finish of 0.3- $\mu\text{m}$  alumina suspension. Image analysis software (ImageJ, National Institutes of Health, Bethesda, MD) was used to determine the area fraction of small Ti-rich particles in the NiTi fiber. Microstructural analysis was conducted using a field emission electron microscope (Hitachi S-4700, Tokyo) at a beam voltage of 15 kV. Backscattered electron imaging was used to increase phase contrast, and EDS point analysis was used to determine phase composition. The WDS analysis was performed on an SEM with a tungsten filament (JEOL\* JXA-8600 Superprobe) at

---

\*JEOL is a trademark of Japan Electron Optics Ltd., Tokyo.

---

15 kV. This was done to verify the EDS data and obtain more accurate quantitative chemical analysis. The standards used for the quantitative WDS analysis were  $\text{TiO}_2$  for Ti, pure Ni for Ni, and pure Sn for Sn. A PET crystal was used for analysis of Ti  $K_{\alpha}$  and Sn  $L_{\alpha}$  peaks, while a ZnF crystal was used for Ni  $K_{\alpha}$ .

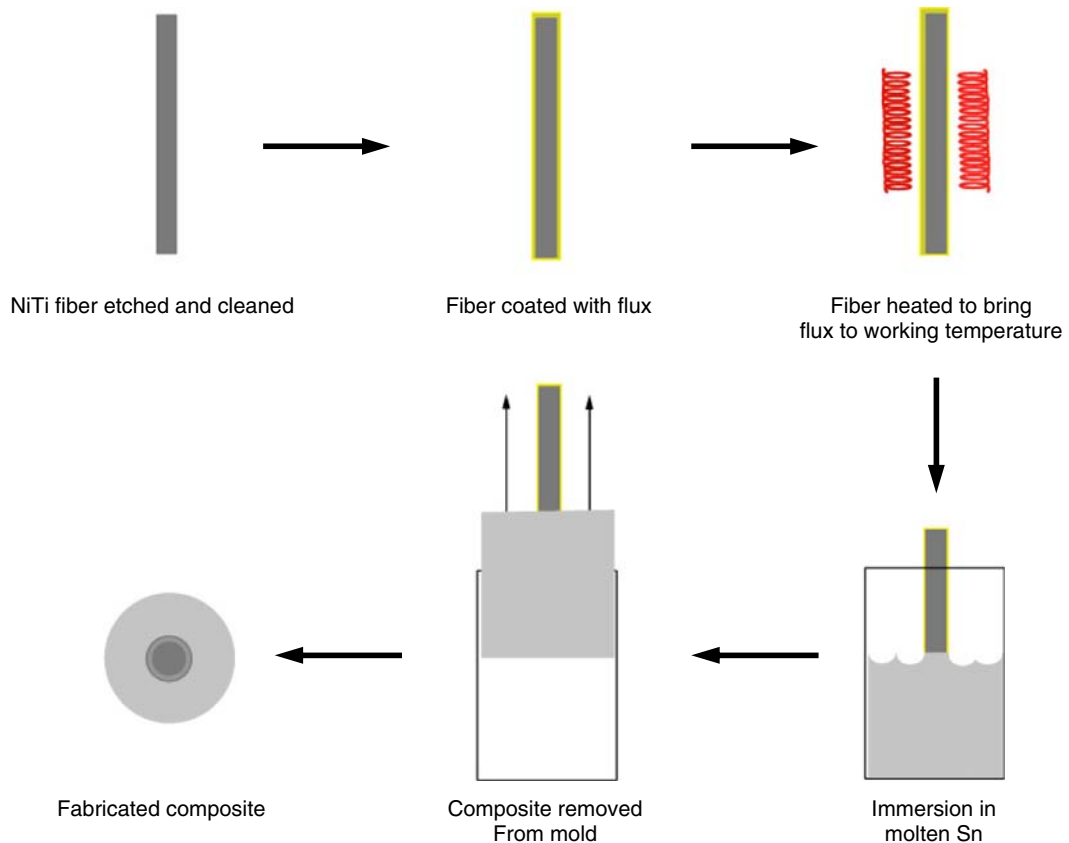


Fig. 1—NiTi-Sn composites were fabricated by immersing etched and fluxed NiTi wire into a 300  $^{\circ}\text{C}$  molten Sn bath for 24 to 168 h in a furnace. After samples were removed from the mold, they were cross sectioned and analyzed to characterize interphase growth.

A commercial nanoindenter (MTS Nano XP-II, Minneapolis, MN) was used to measure Young's modulus and hardness of the different phases. Indentations were performed with a Berkovich indenter (three-sided pyramid) to a depth of 900 nm at a nominal strain rate of 0.05/s. The properties of the NiTi fiber, Sn matrix, and the reaction products between fiber and matrix were examined. Approximately 50 indentations were conducted in each component of the microstructure. In order to more accurately probe the mechanical response of small microstructural features with limited contribution from the surrounding microstructure, a dynamic contact module (DCM) was used. The DCM has an increased displacement resolution, which allows for accurate measurements to be obtained at small indentation depths (10 to 100 nm). These experiments were also conducted with a Berkovich indenter to a final depth of 400 nm. All indentations were performed using the continuous stiffness measurement technique.<sup>[25]</sup> Here, a small high-frequency harmonic is superimposed over the indentation load to continuously measure the contact stiffness of the sample during loading. From this contact stiffness, the Young's modulus of the material and the hardness can be determined instantaneously as a function of depth. Calibration of the instrument was performed on a reference sample of fused silica. Modulus and hardness data from specific locations were correlated with compositions obtained *via* EDS and WDS to determine the effect of atomic composition on mechanical properties.

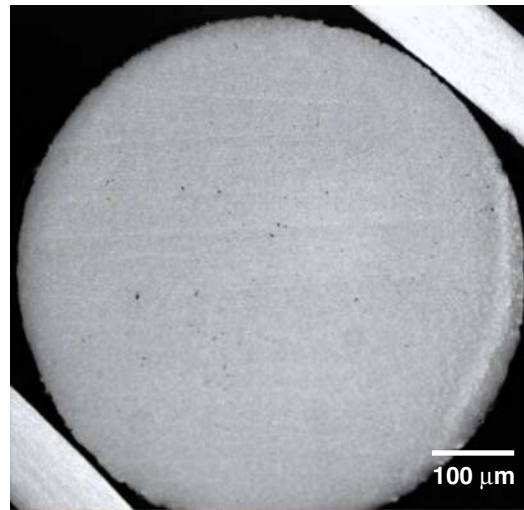
### III. RESULTS AND DISCUSSION

#### A. Microstructure Evolution of NiTi in Liquid Sn

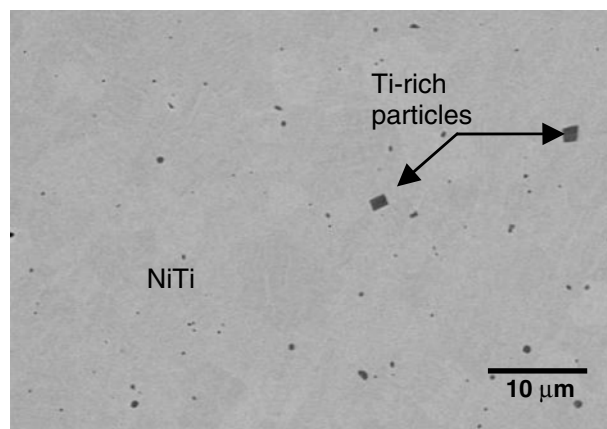
The microstructure of the as-received NiTi fiber was characterized by SEM and EDS (Figure 2). The average grain size of the fiber was approximately 5  $\mu\text{m}$ . The EDS analysis of the fiber showed the composition to be similar to that reported by the manufacturer. Small Ti-rich particles were observed within the NiTi fiber. These had an average diameter of about 0.5  $\mu\text{m}$ . The volume fraction of the particles in the fiber was approximately 0.4 pct. The evolution of the microstructure of the NiTi fiber-reinforced Sn matrix composites aged in liquid Sn at 300  $^{\circ}\text{C}$  for up to 168 hours is shown in Figure 3. Two distinct phases are present: (1) a continuous phase at the interface between the NiTi fiber and molten tin, and (2) growth of a discontinuous phase at the periphery of the first phase and in contact with liquid Sn, after approximately 72 hours (Figure 4).

The EDS and WDS analyses were used to quantify the composition across both interfacial layers. It is instructive to use the Andersen–Hasler relation<sup>[24]</sup> to determine the interaction volume for both EDS and WDS analyses. The X-ray generating radius for a given element,  $R$ , is given by

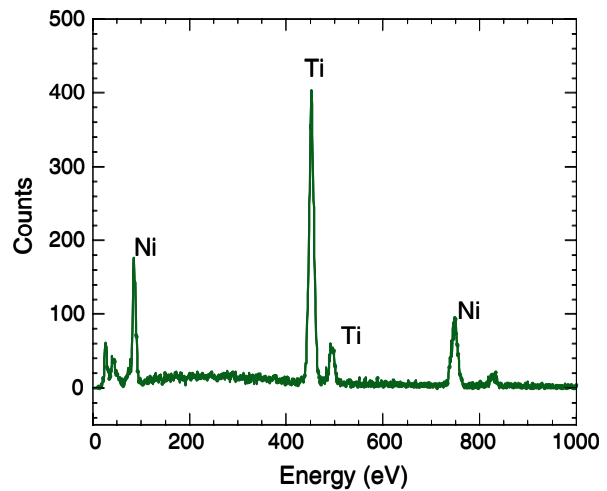
$$R = \frac{0.064(E_o^{1.68} - E_c^{1.68})}{\rho}$$



(a)



(b)



(c)

Fig. 2—(a) Microstructure analysis of NiTi wire reveals (b) binary NiTi with a grain size of approximately 5  $\mu\text{m}$  in diameter and Ti-rich particles on the order of 0.5  $\mu\text{m}$  in diameter and 0.3 to 0.5 pct. (c) EDS analysis of a Ti-rich particle in the NiTi matrix. Note that quantitative compositional calculations were not made due to the small particle size.

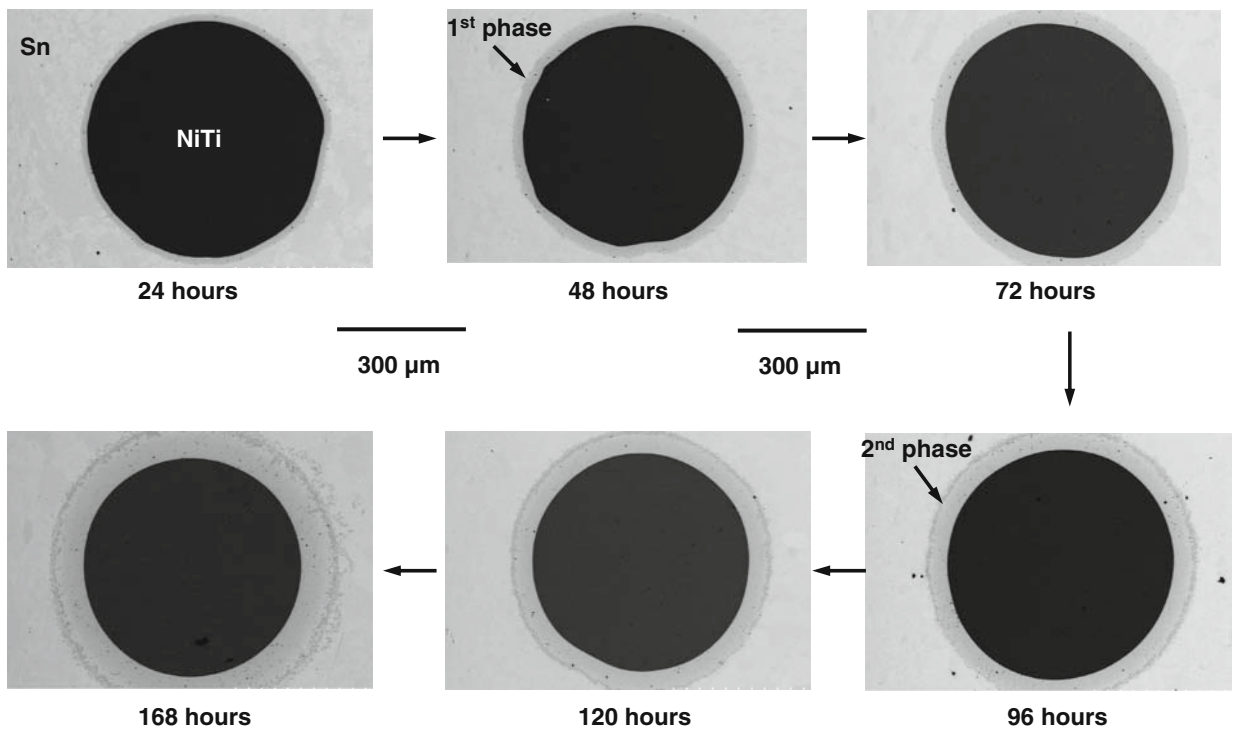


Fig. 3—Formation of NiTi/Sn interphases over 168 h immersion at 300 °C shows growth of two interphases, one beginning at 72 h and the other beginning at 120 h.

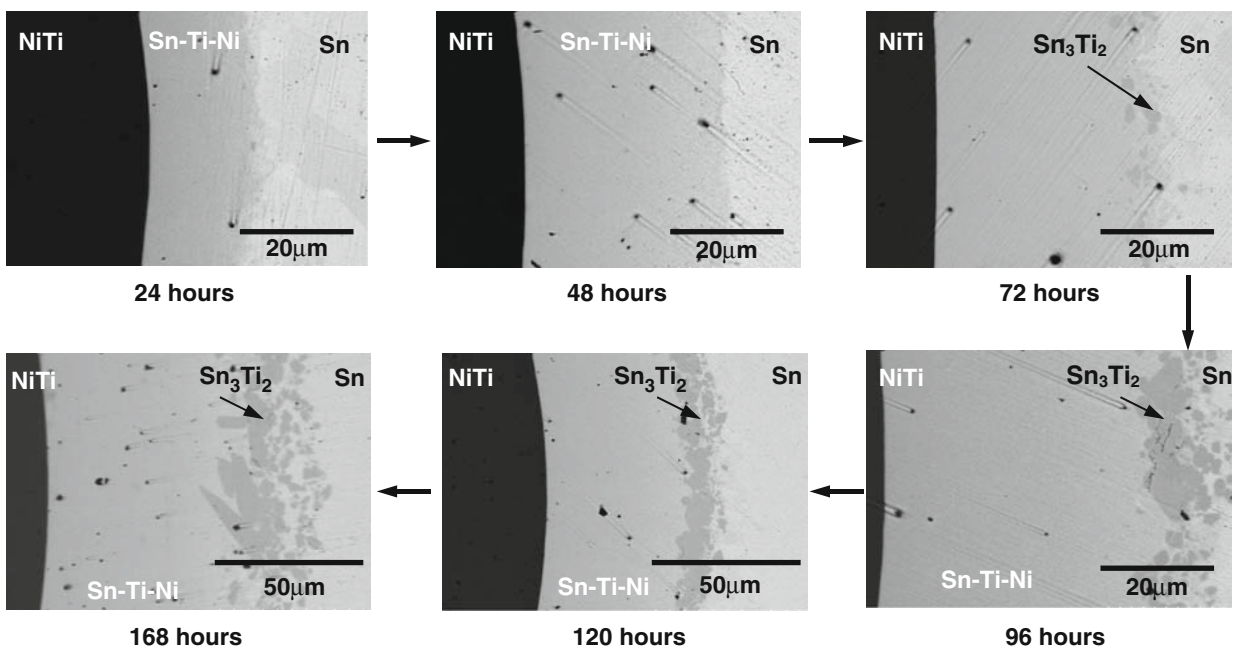


Fig. 4—Higher magnification of interphase growth over 168 h immersion at 300 °C shows formation of two interphases, a Sn-Ti-Ni ternary, and  $\text{Sn}_3\text{Ti}_2$  visible after 72 h. Note that the micrographs at 120 and 168 h are at a lower magnification.

where  $E_o$  is the electron voltage (keV),  $E_c$  is the characteristic X-ray energy (keV) of the element of interest, and  $\rho$  is the density ( $\text{g}/\text{cm}^3$ ) of the material. This estimation determines the electron range by combining

effects of elastic scattering and energy loss due to inelastic scattering. Clearly, the radius is dependent on the density of the material being examined. Pure Sn has a density of about  $7.3 \text{ g}/\text{cm}^3$ , while  $\text{Sn}_3\text{Ti}_2$  has a density

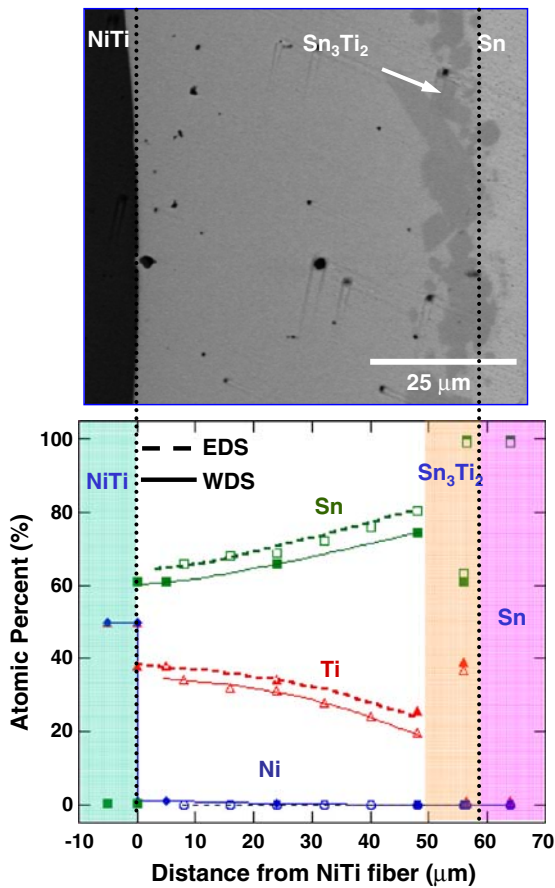


Fig. 5—Comparison of EDS and WDS data with a micrograph of the interphases. The EDS and WDS analyses reveal a variation in composition within the inner Ni-Ti-Sn phase of the composite and a  $\text{Sn}_3\text{Ti}_2$  intermetallic for the outer phase. Additionally, WDS microprobe analysis shows Ni present in the first 20  $\mu\text{m}$  of the Sn-Ti-Ni phase.

of  $7.2 \text{ g/cm}^3$  (calculated from data given in O'Brien *et al.*<sup>[28]</sup>). Assuming a simple rule of mixtures, the density of 62Sn-38Ti and 82Sn-18Ti is between  $6.2$  and  $6.8 \text{ g/cm}^3$ , respectively. Over this range of densities, the Andersen-Hasler X-ray generation radii for Sn  $L_{\alpha_2}$ , Ti  $K_{\alpha_2}$ , and Ni  $K_{\alpha}$  were calculated to be  $0.76$  to  $0.89 \mu\text{m}$ ,  $0.72$  to  $0.84 \mu\text{m}$ , and  $0.57$  to  $0.67 \mu\text{m}$ , respectively. Because the solid solution layer was at least  $20\text{-}\mu\text{m}$  thick, and measurements on the  $\text{Sn}_3\text{Ti}_2$  were conducted on particles about  $20\text{-}\mu\text{m}$  thick, the interaction volumes are much smaller than the region being analyzed.

The EDS and WDS analyses across the interfacial region show that the inner phase contains approximately 60 pct Sn, 40 pct Ti, and 1 pct Ni at the fiber surface and progressively becomes richer in Sn and poorer in Ti and Ni with increasing distance from the fiber (Figure 5). Thus, the inner layer appears to be a solid solution of Sn-Ti-Ni. Indeed, the backscattered SEM images show that the contrast varies continuously in the first layer, being darkest close to the NiTi wire and progressively getting lighter with increasing distance from the fiber. The outer reaction layer had a different morphology and a constant composition of approximately 63 pct Sn and 37 pct Ti. There was no Ni detected in the outer layer by either the EDS or WDS technique. Thus, based on these observations and the Sn-Ti phase diagram, this outer phase appears to be a stoichiometric compound of  $\text{Sn}_3\text{Ti}_2$  (Figure 6). Kuper *et al.*<sup>[26]</sup> discovered that a  $\text{TiSn}_x$  phase forms between liquid Sn and pure Ti and has a Sn to Ti ratio of approximately 1.5. Further studies confirmed the composition of this phase to be  $\text{Sn}_3\text{Ti}_2$ .<sup>[27,28]</sup> Note that at the aging temperature, on the Sn-rich part of the phase diagram, there is a two-phase region where  $\text{Sn}_3\text{Ti}_2$  and liquid Sn coexist, in agreement with our observations.

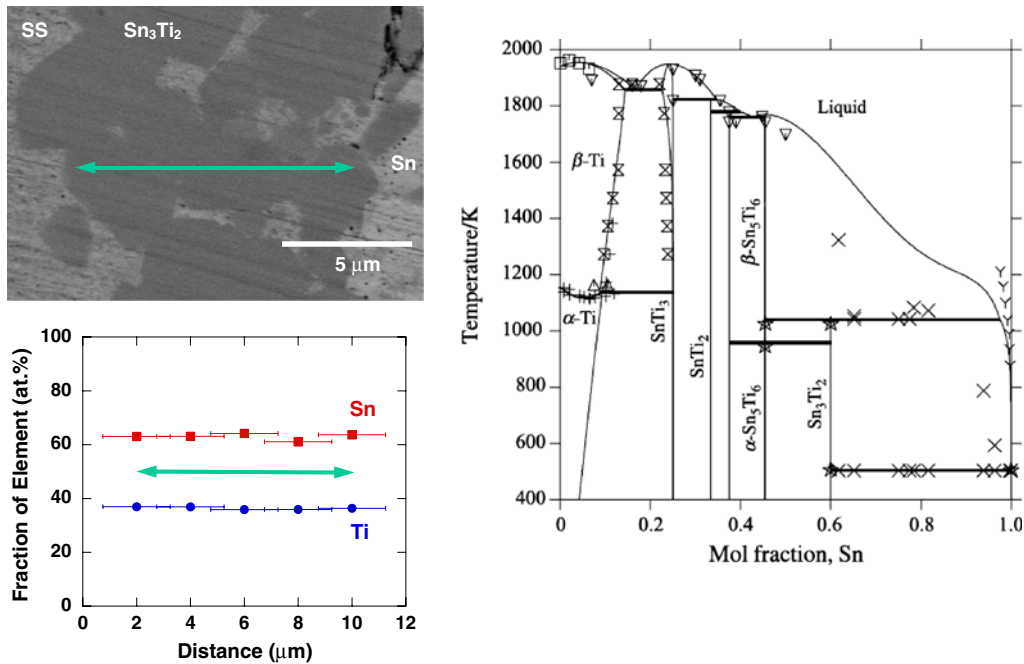


Fig. 6—Sn-Ti binary phase diagram showing  $\text{Sn}_3\text{Ti}_2$  intermetallic formation at 0.6 mol pct Sn.<sup>[28]</sup>

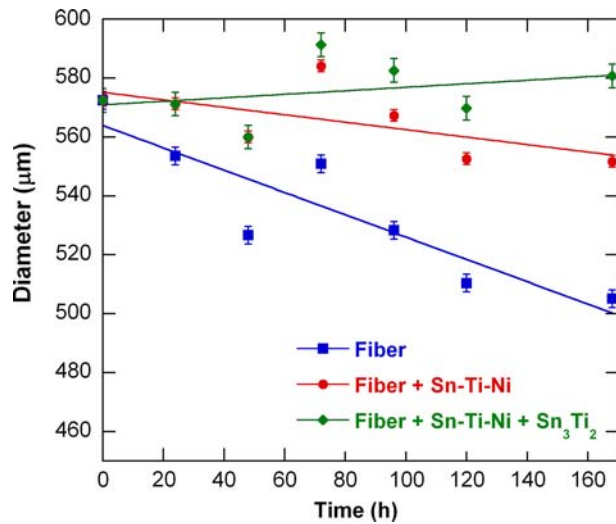


Fig. 7—Thickness of various aspects of Ni-Ti-Sn microstructure over time at 300 °C show initial net diffusion into the wire, followed by formation of  $\text{Sn}_3\text{Ti}_2$  intermetallic growing out into the liquid Sn.

The evolution of the diameter of the NiTi fiber and thickness of each interphase gives additional insight into the possible diffusion mechanisms taking place (Figure 7). The NiTi fiber diameter decreases with increasing aging time, while the thickness of the inner and outer layers increases. A schematic illustrating the proposed diffusion mechanisms during aging is shown in Figure 8. Initially, Sn, Ti, and Ni interdiffuse to form Sn-Ti-Ni solid solution. The growth front moves into the fiber, so Sn diffuses faster into the fiber than Ti can diffuse into liquid Sn. It is interesting to note that the presence of Ni within the intermediate layer causes it to remain as a solid solution of Sn-Ti-Ni. At the periphery of this layer, as soon as the Ni concentration goes to zero,  $\text{Sn}_3\text{Ti}_2$  is formed from the reaction between Sn and Ti (as described by the binary Sn-Ti phase diagram).

### B. Mechanical Properties of Interfacial Products by Nanoindentation

Nanoindentation was used to correlate the mechanical properties of the interfacial layers with the measured composition through the microstructure. Indentations in NiTi, Sn, Sn-Ti-Ni solid solution, and  $\text{Sn}_3\text{Ti}_2$  intermetallic were conducted. A strong relationship between composition and measured hardness/modulus was observed. Figure 9 shows indentations in the Sn-Ti-Ni solid solution layer. The Young's modulus and hardness vs indentation depth are also shown. The modulus and hardness are essentially constant over the indentation depth. Note that with increasing distance from the NiTi fiber, *i.e.*, an increase in the amount of Sn (decrease in Ti), the Young's modulus and hardness decrease.

Indentations in the  $\text{Sn}_3\text{Ti}_2$  intermetallic are shown in Figure 10. Note that the indentation is well within the intermetallic particle (the small microcracks are due to polishing and were not observed in all intermetallic

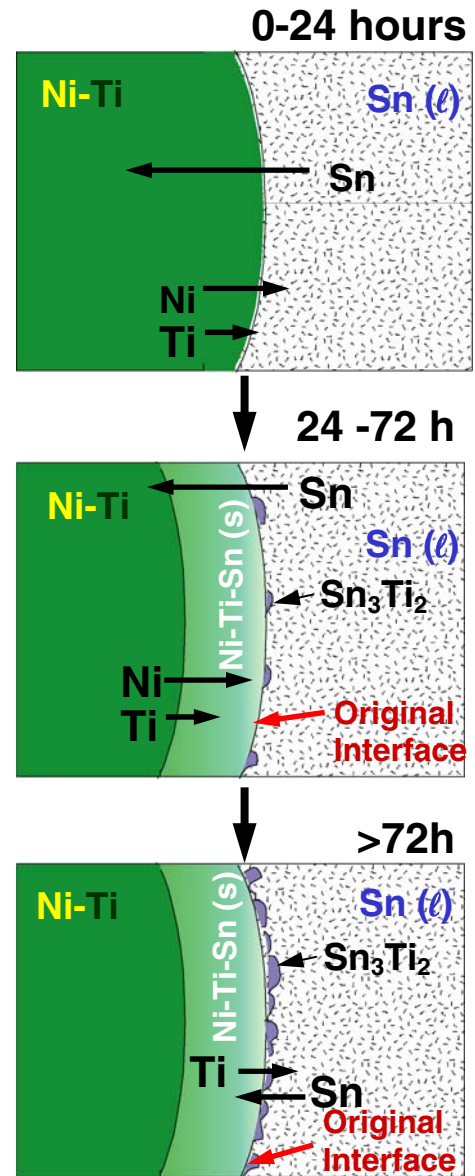


Fig. 8—Schematic illustrating the diffusion characteristics of the Ni-Ti-Sn system at 300 °C. Initial interdiffusion of Sn, Ni, and Ti creates a ternary Ni-Ti-Sn phase with 1.0 at. pct solubility of Ni. After 72 h, the amount of Ni at the growth front is low enough to enable outward growth of the binary  $\text{Sn}_3\text{Ti}_2$  intermetallic.

particles). Particular care was taken to extract modulus and hardness information at shallower depths (50 to 100 nm) where a “plateau” was present. The reason is that at larger depths the intermetallic islands were somewhat prone to “sink” in the Sn matrix. This was captured by sharp decreases in modulus and hardness at larger indentation depths (>200 nm). Figure 10 shows the location of indentations in the  $\text{Sn}_3\text{Ti}_2$  intermetallic. Figure 11 shows the modulus and hardness as a function of position, beginning at the NiTi fiber and ending in the pure Sn region. Note that the evolution of composition in Sn-Ti-Ni is directly related to the modulus and hardness. It is interesting to note that the  $\text{Sn}_3\text{Ti}_2$  intermetallic has a higher modulus and hardness than

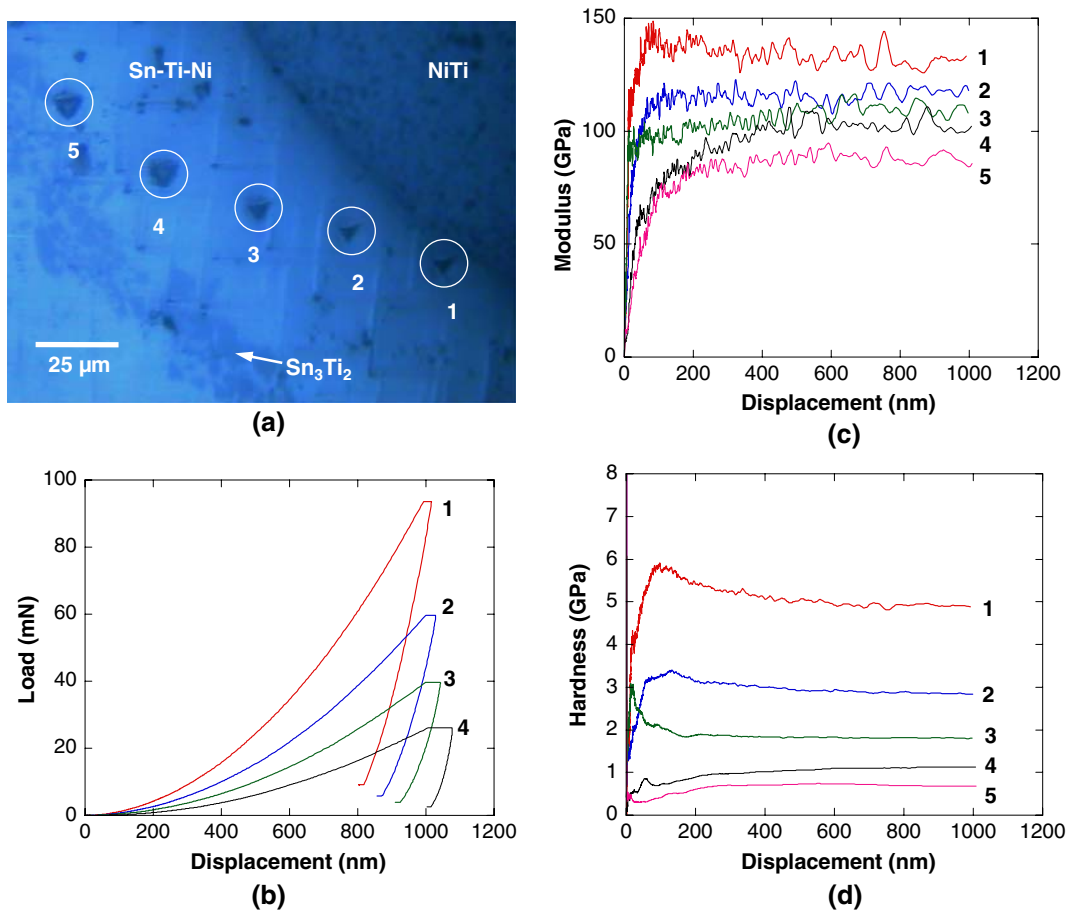


Fig. 9—(a) Indentations in Sn-Ti-Ni solid solution, (b) load displacement, (c) modulus vs displacement, and (d) hardness vs displacement curves for the locations shown in part (a). Note that, as Sn content increases, the modulus and hardness decrease.

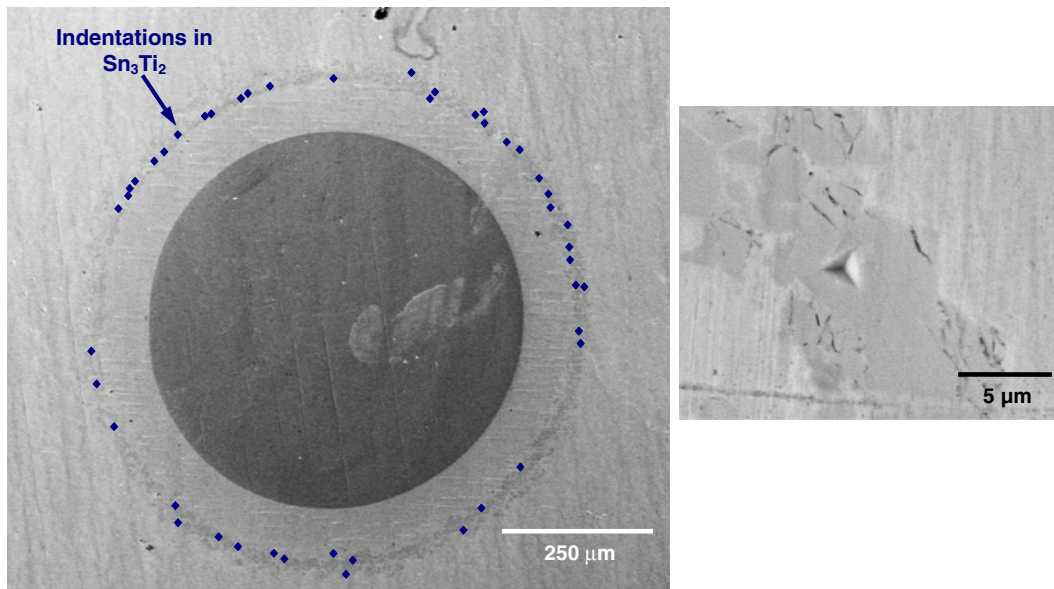


Fig. 10—Locations of nanoindentations performed on Sn<sub>3</sub>Ti<sub>2</sub> intermetallic. Indentations were performed only on the largest nodules and at very shallow depths to reduce the effects from the surrounding matrix.

**Table I. Young's Modulus and Hardness Measured by Nanoindentation**

Material	Young's Modulus (GPa)	Literature Value of Modulus (GPa)	Hardness (GPa)	Literature Value of Hardness (GPa)
NiTi	68.3 ± 1.8	69 ± 5 <sup>[29]</sup>	3.4 ± 0.2	—
Sn	45.5 ± 1.4	46.7 ± 2.7 <sup>[30]</sup>	0.16 ± 0.03	0.22 ± 0.03 <sup>[30]</sup>
Sn <sub>3</sub> Ti <sub>2</sub>	144.3 ± 13.2	—	8.7 ± 0.9	—

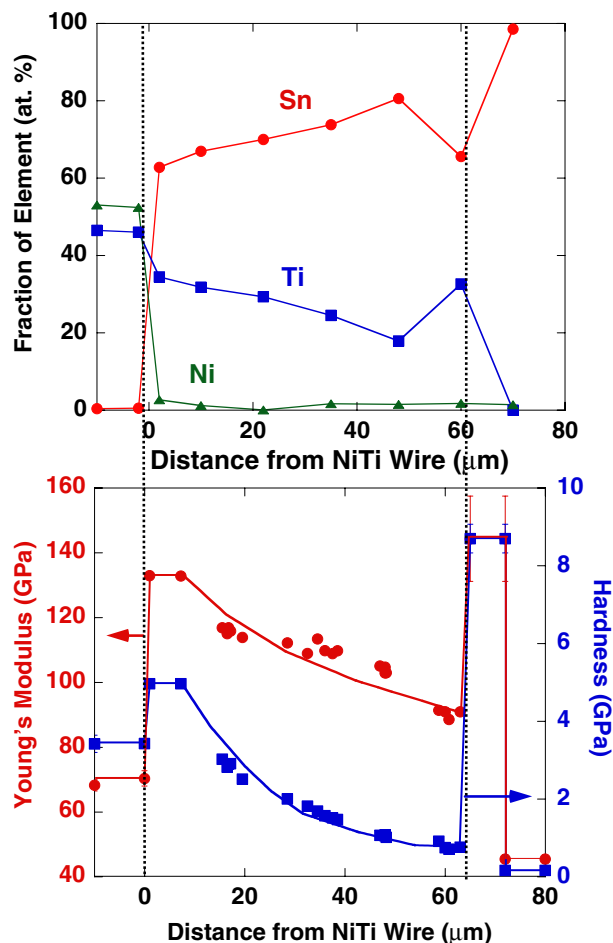


Fig. 11—Correlation between the atomic composition and hardness/modulus of interphases in the Ni-Ti-Sn system.

the Sn-Ti-Ni phase over the entire range of its composition. Furthermore, it is clear that this compound is an intermetallic compound, because both the modulus and hardness are higher than those of the region of the nominally same composition in the solid solution layer. Thus, it is quite clear that the first phase appears to be a Sn-Ni-Ti solid solution and the second is the Sn<sub>3</sub>Ti<sub>2</sub> intermetallic described by Kuper *et al.*<sup>[26]</sup> Table I shows a comparison of the modulus and hardness measured for Sn<sub>3</sub>Ti<sub>2</sub> in our study. A comparison of measurements on NiTi and Sn, with that reported in the literature, shows very good agreement, indicating that the nanoindentation technique used here is quite accurate in probing mechanical properties at small volumes.

#### IV. CONCLUSIONS

We have studied the interfacial reactions between NiTi fibers in a liquid Sn matrix. The relationship between the composition of the interfacial phases and their mechanical properties was investigated. Based on the results of this work, the following conclusions can be made.

1. Immersion of NiTi fiber in liquid Sn at 300 °C for up to 168 hours resulted in two interfacial reaction layers. The EDS and WDS analyses show that the first layer to form is a ternary solid solution of Sn-Ti-Ni. At the periphery of this layer, where the concentration of Ni is close to zero, Sn reacts with Ti to form Sn<sub>3</sub>Ti<sub>2</sub>.
2. Nanoindentation revealed that the hardness and modulus of the Sn-Ti-Ni phase are directly related to composition. The Sn<sub>3</sub>Ti<sub>2</sub> phase had a higher modulus and hardness than the Sn-Ti-Ni phase at a similar composition, suggesting that it is indeed a stoichiometric intermetallic compound.

#### ACKNOWLEDGMENTS

One of the authors (JPC) acknowledges Intel Corporation for an ASU-Intel graduate fellowship. The authors acknowledge the financial support for this research from Intel (Drs. D. Suh, R. Mahajan, and V. Wakharkar). The authors also thank (1) Gordon Moore from the Department of Chemistry and Biochemistry at Arizona State University for his help with the WDS and (2) Memry Corporation for providing the NiTi fibers used in this study.

#### REFERENCES

1. S. Kang and A.K. Sarkhel: *J. Electron. Mater.*, 1994, vol. 23, p. 701.
2. D.R. Frear and P.T. Vianco: *Metall. Mater. Trans. A*, 1994, vol. 25A, p. 1509.
3. J. Glazer: *Int. Mater. Rev.*, 1995, vol. 40, p. 65.
4. M. Abtew and G. Selvaduray: *Mater. Sci. Eng. R*, 2000, vol. 27, p. 95.
5. W.J. Plumridge: *Monatshfte Chem.*, 2005, vol. 136, p. 1811.
6. P.T. Vianco and D.R. Frear: *J. Electron. Mater.*, 1993, vol. 45, p. 14.
7. S. Choi, K.N. Subramanian, J.P. Lucas, and T.R. Bieler: *J. Electron. Mater.*, 2000, vol. 29, p. 1249.
8. S. Terashima, K. Yoshiharu, H. Takuya, and T. Masamoto: *J. Electron. Mater.*, 2003, vol. 32, p. 1527.



9. M.A. Meyers and K.K. Chawla: *Mechanical Behavior of Materials*, Prentice Hall, Upper Saddle River, NJ, 1999.
10. K. Otsuka and C.M. Wayman: *Shape Memory Materials*, Cambridge University Press, Cambridge, United Kingdom, 1998.
11. C.P. Frick, A.M. Ortega, J. Tyber, A. Maksound, H.J. Maier, Y. Liu, and K. Gall: *Mater. Sci. Eng. A*, 2005, vol. 405, p. 34.
12. A. Shimamoto, H.Y. Zhao, and H. Abe: *Int. J. Fatigue*, 2004, vol. 26, p. 533.
13. D. Vokoun, V. Kafka, and C.T. Hu: *Smart Mater. Struct.*, 2003, vol. 12, p. 680.
14. M. Wagner, T. Sawaguchi, G. Kausträter, D. Höffken, and G. Eggeler: *Mater. Sci. Eng. A*, 2004, vol. 378, p. 105.
15. Z.G. Wang, X.T. Zua, Y.Q. Fub, and L.M. Wang: *Thermochimica Acta*, 2005, vol. 428, p. 199.
16. J.M. Young and K.J. Van Vliet: *J. Biomed. Mater. Res.*, 2005, vol. 72, p. 17.
17. Y. Zheng, L. Cui, and J. Schrooten: *Appl. Phys. Lett.*, 2004, vol. 84, p. 31.
18. L.C. Brinson, I. Schmidt, and R. Lammering: *J. Mech. Phys. Solids*, 2004, vol. 52, p. 1549.
19. Z.G. Wei, R. Sandstrom, and S. Miyazaki: *J. Mater. Sci.*, 1998, vol. 33, p. 3763.
20. I. Dutta, B.S. Majumdar, D. Pan, W.S. Horton, W. Wright, and Z.X. Wang: *J. Electron. Mater.*, 2004, vol. 33, p. 258.
21. Z.X. Wang, I. Dutta, and B.S. Majumdar: *Mater. Sci. Eng. A*, 2006, vol. 421, p. 133.
22. Z.X. Wang, I. Dutta, and B.S. Majumdar: *Scripta Mater.*, 2006, vol. 54, p. 627.
23. O. Fouassier, J. Chazelas, and J. Silvain: *Compos. Part A*, 2002, vol. 33, p. 1391.
24. C.A. Anderson and M.F. Hasler: *Proc. 4th Int. Conf. on X-ray Optics and Microanalysis*, R. Castaing, P. Deschamps, and J. Philibert, eds., Hermann, Paris, 1966, pp. 310–27.
25. W.C. Oliver and G.M. Pharr: *J. Mater. Res.*, 2004, vol. 19, p. 3.
26. C. Kuper, W. Peng, A. Pisch, F. Goesmann, and R. Schmid-Fetzer: *Z. Metallkd.*, 1998, vol. 89, p. 855.
27. C. Liu, U.E. Klotz, P.J. Uggowitzner, and J.F. Loeffler: *Monatshefte Chem.*, 2005, vol. 136, p. 1921.
28. J.W. O'Brien, R.A. Dunlap, and J.R. Dahn: *J. Alloys Compd.*, 2003, vol. 353, p. 60.
29. D.C. Dunand, D. Mari, M.A.M. Bourke, and J.A. Roberts: *Metall. Mater. Trans. A*, 1996, vol. 27A, pp. 2820–36.
30. X. Deng, N. Chawla, K.K. Chawla, and M. Koopman: *Acta Mater.*, 2004, vol. 52, pp. 4291–4303.